


Cite this: *Dalton Trans.*, 2024, **53**, 12119

Strategic design and development of a siderophore mimic: pioneering anticancer therapy via ROS generation and ferroptosis†

Abhishek Panwar,^a Anushree Lye,^b Dulal Musib,^a Aarti Upadhyay,^c Irungbam Karankumar,^a Paonam Bebika Devi,^a Maynak Pal,^a Biswanath Maity^{*b,d} and Mithun Roy ^{*a,e}

We designed a tris-catecholate-based siderophore mimic, H₆-T-CATL, to selectively chelate iron(III) from mitochondrial cytochromes and other iron-containing proteins within cellular matrices. This strategic sequestration aims to trigger apoptosis or ferroptosis in cancer cells through the glutathione (GSH)-dependent release of reduced iron and subsequent ROS-mediated cytotoxicity. Synthesis of H₆-T-CATL involved precise peptide coupling reactions. Using the Fe(III)-porphyrin model (Fe-TPP-Cl), akin to cytochrome c, we studied H₆-T-CATL's ability to extract iron(III), yielding a binding constant (K_{rel}) of 10¹⁴ for the resulting iron(III) complex (Fe^{III}-T-CATL)³⁻. This complex readily underwent GSH-mediated reduction to release bioavailable iron(II), which catalyzed Fenton-like reactions generating hydroxyl radicals (•OH), confirmed by spectroscopic analyses. Our research underscores the potential of H₆-T-CATL to induce cancer cell death by depleting iron(III) from cellular metalloproteins, releasing pro-apoptotic iron(II). Evaluation across various cancer types, including normal cells, demonstrated H₆-T-CATL's cytotoxicity through ROS production, mitochondrial dysfunction, and activation of ferroptosis and DNA damage pathways. These findings propose a novel mechanism for cancer therapy, leveraging endogenous iron stores within cells. H₆-T-CATL emerges as a promising next-generation anticancer agent, exploiting iron metabolism vulnerabilities to induce selective cancer cell death through ferroptosis induction.

Received 18th May 2024,
Accepted 29th June 2024

DOI: 10.1039/d4dt01461h

rsc.li/dalton

Introduction

Iron plays a pivotal role in numerous biological processes, including oxygen transport, DNA synthesis, ATP production, and acting as a cofactor for enzymes crucial in cell growth.^{1–5} Cancer cells often manipulate their iron metabolism to sustain their proliferation and survival. Targeting the disrupted iron homeostasis as a strategy to impede cancer progression has emerged as an attractive strategy for cancer therapy.^{6–10} To this end, the development of iron chelators as therapeutic agents

has gained attention, initially intended for managing iron overload. Later the iron(III)-chelators revealed their efficacy in hindering tumor growth through various mechanisms such as cell cycle regulation and angiogenesis suppression.^{11,12} Siderophores, chelators produced by bacteria and fungi to scavenge iron, have emerged as potential candidates for iron chelation therapy in cancer.^{13–15} Natural and synthetic siderophores like deferoxamine (DFO) and deferasirox have exhibited promising anticancer properties by limiting iron availability to malignant cells.^{16–18} Nonetheless, their clinical advancement has been hampered by significant side effects and limited efficacy, necessitating the quest for more potent and selective iron chelators tailored for cancer treatment. While iron chelation therapy is established for managing systemic iron excess, its efficacy in improving survival outcomes for cancer patients remains inconclusive.¹⁹ Excessive intracellular iron levels can induce ferroptosis, a form of cell death characterized by lipid peroxidation due to oxidative stress, which has garnered attention as a potential therapeutic avenue in cancer management.^{20–23} Strategies aimed at enhancing ferroptosis induction represent a promising approach to augment the effectiveness of chemotherapy, particularly by exploiting non-

^aDepartment of Chemistry, National Institute of Technology Manipur, Langol, Imphal West, 795004 Manipur, India. E-mail: mithunroy@nitmanipur.ac.in

^bDepartment of Systems Biology, Center of Biomedical Research (CBMR), Raebareli Road, Lucknow 226014, Uttar Pradesh, India. E-mail: bmaity@jcbse.ac.in

^cDepartment of Inorganic and Physical Chemistry, Indian Institute of Science Bangalore, Bangalore-50012, Karnataka, India

^dDepartment of Biological Sciences, Bose Institute Unified Academic Campus, EN80, Sector V, Bidhan Nagar, Kolkata - 700091, West Bengal, India

^eDepartment of Chemistry, National Institute of Technology Agartala, Jirania, West Tripura, Agartala, 799046, India

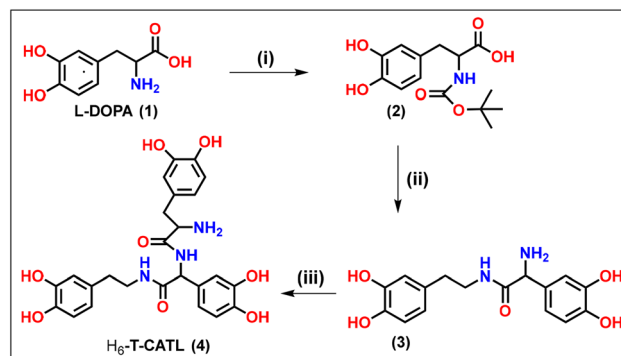
† Electronic supplementary information (ESI) available. See DOI: <https://doi.org/10.1039/d4dt01461h>

apoptotic cell death pathways associated with reactive oxygen species accumulation and lipid peroxidation.^{24,25} Research into ferroptosis inducers has seen a significant surge, with numerous methods for inducing ferroptosis in cancer treatment extensively investigated. These methods include the utilization of small molecules such as erastin, sorafenib (SRF), and sulfasalazine (SAS), or shMTHFD2 and shGPX4 plasmids those target related genes.^{26–30} However, existing ferroptosis inducers encounter challenges due to their low water solubility and instability, limiting their applicability in cancer therapy.³¹ Moreover, hurdles in clinical translation include their limited therapeutic efficacy, notable side effects, and difficulties in detection.³² Furthermore, the substantial adverse effects associated with iron chelation and ferroptosis inducers pose significant barriers to their utilization in cancer therapy. To address the limitations, our study focuses on the development of a catechol-based siderophore mimic capable of chelating endogenous iron(III) of an intracellular matrix, facilitating its reduction to iron(II) by glutathione (GSH) or other reducing equivalents, and subsequently inducing ferroptosis/apoptosis through the generation of reactive oxygen species (ROS) *via* Fenton-like chemistry to kill the cancer cells (Scheme 1). Therefore, we present the synthesis and characterization of a tris catechol ligand (H_6 -T-CATL), designed as a mimic of catecholate-based siderophores, as a potential iron chelation strategy along with investigations including iron(III) leaching by H_6 -T-CATL, reduction of Fe(III) and iron(II) release studies in the presence of GSH, GSH depletion assays, hydroxyl radical generation assays, BSA-binding studies, cell viability assays, *in vitro* ROS-generation, apoptosis, protein expression studies for the complete validation of the hypothesis.

Results and discussion

Synthesis, characterization, and general aspects

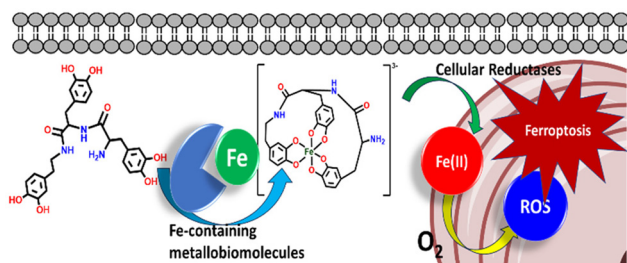
In accordance with the previously reported synthesis procedure, the tris-catechol ligand (H_6 -T-CATL), was synthesized (Scheme 2).^{33,34} The synthesis involved a series of steps beginning with the protection of the amine group in L-Dopa using di-*tert*-butyl dicarbonate (Boc) (i), followed by peptide coupling with dopamine hydrochloride in the presence of 1-ethyl-3-(3-dimethylaminopropyl)carbodiimide (EDC),



Scheme 2 Schematic drawings of the synthesis of catecholate-based ligand (H_6 -T-CATL). (i) Boc_2O , 1 M NaOH, 24 h; (ii) L-Dopa·HCl, 1-ethyl-3-(3-dimethylaminopropyl)carbodiimide (EDC), HOBT, diisopropyl ethylamine (DIPEA), 0–5 °C, 72 hours; trifluoroacetic acid, 40 °C, 2 h; (iii) Boc-protected L-Dopa (2), EDC, HOBT, DIPEA, 0–5 °C, 72 hours; trifluoroacetic acid, 40 °C, 2 h.

hydroxybenzotriazole (HOBT), and trimethylamine (ii). After the isolation of the product, the protected amine group was deprotected utilizing trifluoroacetic acid (TFA). Later, the free amine group in the initial peptide-coupling product underwent further EDC coupling with Boc-(NH₂)-protected L-Dopa to yield the Boc-(NH₂)-protected tris catecholate ligand, which was deprotected using TFA to furnish the free amino tris catecholate ligand (H_6 -T-CATL) (iii). The synthesized compound was characterized using infrared (IR) and mass (Fig. S1 and S2[†]). To assess the solubility of H_6 -T-CATL in a biologically relevant medium, a 5% DMSO–PBS buffer solution was employed. The H_6 -T-CATL exhibited high solubility in this medium, suggesting its potential suitability for biological applications. The stability of H_6 -T-CATL was evaluated under physiological conditions, specifically in a 5% DMSO–PBS buffer at pH 7.4 and room temperature through UV-visible spectroscopy, which revealed the remarkable stability till 72 h. This stability profile underscored the reliability of H_6 -T-CATL as a candidate ligand for further investigation and development in various biomedical contexts.

The distribution of pharmaceutical compounds within tissues is influenced by their lipophilicity, a critical parameter known as the logarithm of the partition coefficient ($\log P$). This characteristic, which measures the compound's propensity to partition between a hydrophobic solvent (such as *n*-octanol) and water, is crucial for assessing drug distribution and cellular uptake. We calculated the $\log P$ value for the tris catecholate ligand (H_6 -T-CATL) in a 5% DMSO–water mixture, as well as in comparison to *n*-octanol. The average $\log P$ value obtained for H_6 -T-CATL was determined to be 0.41. This positive value suggests that H_6 -T-CATL possesses a favourable affinity for lipids and hydrophobic environments, which may facilitate its cellular uptake and distribution. Thus, the $\log P$ value underscored the potential of the tris catecholate ligand (H_6 -T-CATL) as a promising candidate for further investigation and development in biomedical applications, where efficient cellular uptake is crucial for therapeutic efficacy.

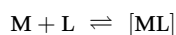


Scheme 1 Proposed hypothesis of the mechanism of induction of ferroptosis in cancer cells by the catecholate-based ligand (H_6 -T-CATL).

We synthesized the iron(III) complex of the 5,10,15,20-tetra-*p*-tolylporphyrin (TPTP) as a model for the intracellular iron-heme proteins, and we probed the chelating/leaching properties of the H₆-T-CATL from the endogenous iron(III)-heme proteins. The synthesis of 5,10,15,20-tetra-*p*-tolylporphyrin (TPTP) was carried out following a previously published protocol.³⁵ The synthesized Fe(III) complex with TPTP was characterized using UV and mass spectroscopy techniques, providing spectral data indicative of its structural identity and purity. This synthesis of [Fe^{III}TPTP-Cl·4H₂O] involved refluxing the porphyrin TPTP and FeCl₂·4H₂O in a DMF which resulted in a dark brown solution at the end of the reaction.³⁶ Characterization of [Fe^{III}TPTP-Cl·4H₂O] was conducted using UV, and mass spectroscopy techniques, providing valuable insights into its structural and chemical properties (Fig. S5 and S6†). We synthesized an iron(III)-catecholate complex (Fe) to elucidate the release of iron after its leaching from the [Fe^{III}TPTP-Cl·4H₂O] by the catecholate ligand (H₆-T-CATL), resulting in the formation of an anionic iron-catecholate complex (Fe^{III}T-CATL)³⁻. The synthesis involved the addition of six equivalents of triethylamine to a methanolic solution of ligand (H₆-T-CATL), followed by the gradual addition of this solution to a methanolic solution of [Fe(NO₃)₃·9H₂O] under an inert atmosphere of nitrogen (N₂). The color of the solution changed to dark purple, and precipitation occurred upon the dropwise addition of diethyl ether, resulting in the formation of complex, (NEt₃H)₃(Fe^{III}T-CATL) with a yield of 30%. Characterization of (NEt₃H)₃(Fe^{III}T-CATL) was carried out using IR, UV-visible, and mass spectroscopy techniques, as illustrated in Fig. S7–S9.† Notably, the solubility and stability of the (NEt₃H)₃(Fe^{III}T-CATL) was probed in 5% DMSO–PBS buffer medium (pH 7.4).

Chelation studies

To assess the binding affinity of H₆-T-CATL towards ferric iron, we calculated the relative stability constant or relative formation constant of the (Fe^{III}T-CATL)³⁻ using a previously established protocol.³⁷ The UV-visible spectrophotometric titrations were conducted, wherein varying concentrations of Fe(III) were added to the H₆-T-CATL in a 1:1 stoichiometry until reaching equilibrium. The relative binding constant (*K*_{rel}) was determined utilizing the Benesi–Hildebrand method, shedding light on the efficacy of H₆-T-CATL as an iron chelator with potential implications for cancer therapy, *i.e.*



$$K = \frac{[ML]}{[M][L]}$$

Utilizing the derived equation and substituting the values of metal and ligand concentrations, we determined the relative binding constant for the tris catecholate ligand (H₆-T-CATL) with Fe(III), yielding a *K*_{rel} value of 1.58 × 10¹⁴ M⁻¹ (Fig. S11†). Remarkably, this binding constant aligns closely with values for iron-known catecholate chelators.³⁸ This finding underscores the robust binding affinity of H₆-T-CATL towards iron,

rendering it a promising candidate for iron chelation therapy. Such enhanced binding ability for iron suggests that H₆-T-CATL may effectively sequester iron ions in an intracellular matrix, offering potential therapeutic benefits in the context of iron-related disorders, including cancer. Moreover, iron also acts as a cofactor for several enzymes crucial in cell growth during cancer progression. In this context, we propose a novel strategy aimed at reducing iron levels and disrupting mitochondrial function by leaching iron from iron-containing metalloproteins using the iron-chelating tris-catecholate ligand (H₆-T-CATL). For our investigation, we selected the iron-containing metalloprotein [Fe^{III}TPTP-Cl·4H₂O], regarded as a cytochrome mimic, to demonstrate the iron(III)-the leaching capability of the tris-catecholate chelating ligand (H₆-T-CATL) (Fig. 1). The leaching of iron(III) from [Fe^{III}TPTP-Cl·4H₂O] complex was evaluated through UV-visible spectral titrations in PBS buffer respectively in pH 5.5 and 7.4, with H₆-T-CATL served as the titrant added to the [Fe^{III}TPTP-Cl·4H₂O]. Upon gradual increase in ligand concentration, a new Q band emerged at 665 nm, primarily attributed to the π–π* transition in a free protonated porphyrin (H₂TTP) once iron was removed from the porphyrin core. Additionally, a peak at around 570 nm, indicative of the newly generated LMCT band, signified the chelation of iron by the catecholate ligand, a phenomenon consistent with prior literature.^{39,40} The emergence of these new bands at 665 and 570 nm not only validates our approach for iron leaching from [Fe^{III}TPTP-Cl·4H₂O] but also confirms the enhanced binding affinity of the catecholate ligand (H₆-T-CATL) toward iron(III).

GSH-assisted reduction of iron(III) and release of iron(II)

Glutathione (GSH) is a well-known antioxidant and mild reducing agent that is often highly expressed in cancer cells to counteract oxidative stress. Understanding the remarkable iron(III)-leaching capability of the H₆-T-CATL, we presumed the formation of the iron(III)-catecholate complex (Fe^{III}T-CATL)³⁻. To

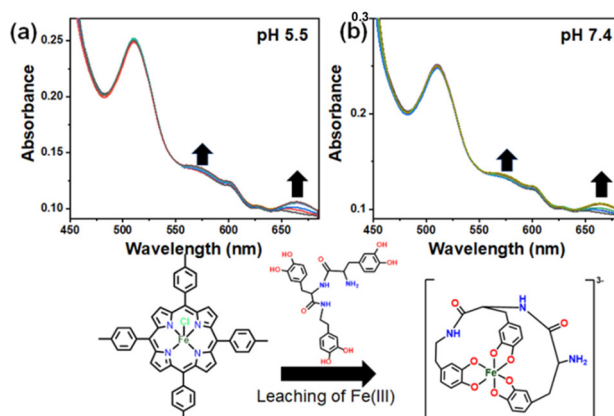


Fig. 1 UV-visible spectral traces revealing leaching of iron(III) from [Fe^{III}TPTP-Cl·4H₂O] complex (0.3 mM) by H₆-T-CATL (0–5 mM) studied in 5% DMSO–PBS buffer medium at (a) intracellular pH 5.5 and (b) extracellular pH 7.4 and room temperature.

understand the fate of iron(III) in a catechol-bound state under the influence of the reducing matrix of the cancer cells, we synthesized and characterized $(\text{NEt}_3\text{H})_3(\text{Fe}^{\text{III}}\text{T-CATL})$ and probed the chemistry in the presence of glutathione. Successive addition of glutathione (0.1–10 mM) at pH 5.5 and 7.4 (Fig. S13†).

Under reducing conditions, we observed a decrease in absorbance of the LMCT band at 570 nm, indicating degradation of the $(\text{Fe}^{\text{III}}\text{T-CATL})^{3-}$, reduction of Fe(III) into Fe(II), and liberation of iron, although there was an insignificant effect on the UV-visible spectra of the $(\text{Fe}^{\text{III}}\text{T-CATL})^{3-}$ in the absence of glutathione. Most probably the iron(III) in the complex was reduced to Fe(II) by glutathione making the complex unstable which led to the release of iron(II) in the solution in the unbound form. To ascertain the presence of unbound iron(II), UV-visible titrations were performed using a mixture of $(\text{Fe}^{\text{III}}\text{T-CATL})^{3-}$ (1 equivalent) and 1,10-phenanthroline (3.0 equivalent) in the presence of increasing concentrations of GSH at pH 5.5 and 7.4. Phenanthroline was utilized as a probe for detecting free Fe^{2+} ions. We observed the appearance of a typical MLCT band of $[\text{Fe}(\text{phen})_3]^{2+}$ centered at 515 nm in the UV-visible spectra.⁴¹ The control UV-visible spectra of the $[\text{Fe}(\text{phen})_3]^{2+}$ under the similar experimental condition confirmed the MLCT band at 515 nm (Fig. S19†). The MLCT band became more intense with the increasing concentrations of GSH (Fig. 2). The typical assay confirmed the release of iron as Fe^{2+} in the presence of GSH. Subsequently, the normalized percentage release of Fe^{2+} concerning different

GSH concentrations was determined using a calibration curve of $[\text{Fe}(\text{phen})_3]^{2+}$ complex. The percentage release of Fe^{2+} at pH 5.5 was approximately 83%, while at pH 7.4, it was approximately 80%. There was no effect of pH on the release of iron(II). A little higher release of iron(II) from the reduced $(\text{Fe}^{\text{III}}\text{T-CATL})^{3-}$ could be due to the effect of protonation. The reductive release of iron from the $(\text{Fe}^{\text{III}}\text{T-CATL})^{3-}$ complex was also confirmed by cyclic voltammetric assays in which a dimethyl formamide (DMF) solution of the $(\text{Fe}^{\text{III}}\text{T-CATL})^{3-}$ (1.0 equivalent) in the presence of 3.0 equivalent of 1,10-phenanthroline using 0.1 M TBAP (tetrabutylammonium perchlorate) as the supporting electrolyte, with glassy carbon serving as the working electrode, Ag/AgCl as the reference electrode, and Pt as the counter electrode was used. In a mixture of We introduced a mixture of $(\text{Fe}^{\text{III}}\text{T-CATL})^{3-}$ (0.03 mM) and 1,10-phenanthroline (0.02 mM), the GSH was added in an increasing concentration and cyclic voltammetric responses were recorded with a scan rate of 50 mV s^{-1} . We observed the development of characteristic peak potentials of $[\text{Fe}(\text{phen})_3]^{2+}$ at 1.3 V and 1.2 V (Fig. 3 and Fig. S20†).⁴² The electrochemical assays provide further evidence that in the presence of GSH, the $(\text{Fe}^{\text{III}}\text{T-CATL})^{3-}$ releases iron in the form of Fe^{2+} . This strategy of leaching iron from metalloproteins and releasing it as Fe^{2+} in a GSH-rich cancerous environment presented a promising approach for activating ferroptosis *via* ROS generation. EPR spectra of $(\text{Fe}^{\text{III}}\text{T-CATL})^{3-}$ was recorded in 5% DMSO–PBS buffer medium at 77 K, and exhibited typical signature of high-spin iron(III) with $g = 4.3$. The addition of GSH signifi-

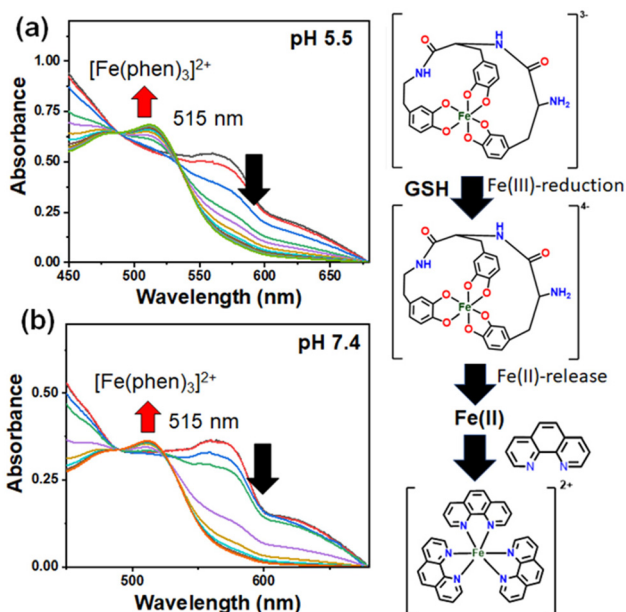


Fig. 2 UV-visible spectral traces indicating the release of iron(II) and the formation of $[\text{Fe}(\text{phen})_3]^{2+}$ (MLCT band at 515 nm) in the presence of increasing concentration of GSH (0–10 mM) and 1,10-phenanthroline (0.09 mM) from the $(\text{Fe}^{\text{III}}\text{T-CATL})^{3-}$ (0.03 mM) in 5% DMSO–PBS buffer medium at (a) intracellular pH 5.5 and (b) extracellular pH 7.4 and room temperature.

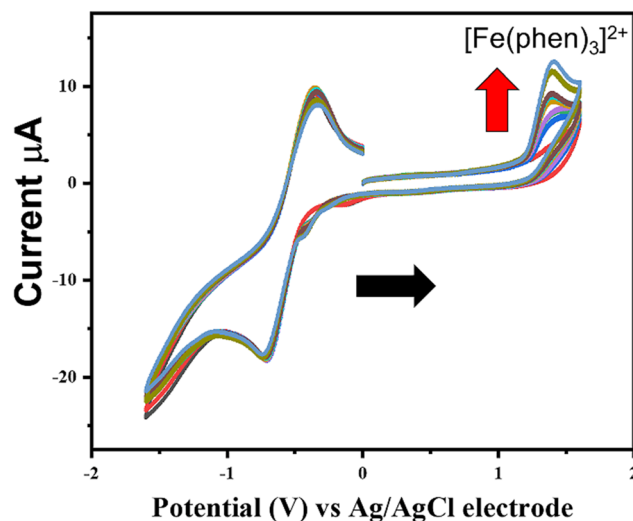


Fig. 3 Cyclic voltammograms of 0.3 mM of $(\text{Fe}^{\text{III}}\text{T-CATL})^{3-}$ recorded in the presence of 1,10-phenanthroline (0.9 mM) and increasing concentration of GSH (0–10 mM) increasing concentrations of GSH in dimethylformamide (DMF) at room temperature (RT) using glassy carbon electrode as working electrode, Ag/AgCl electrode as reference electrode, and Pt electrode as counter electrode and TBAP (tetrabutylammonium perchlorate) 0.1 M as supporting electrolyte, scan rate 50 mV s^{-1} . Appearance of typical Fe(II)/Fe(III) responses of $[\text{Fe}(\text{phen})_3]^{2+}$ at 1.3 V suggested release of Fe(II) from the reduced $(\text{Fe}^{\text{III}}\text{T-CATL})^{3-}$.

cantly reduced the EPR signal indicating reduction of Fe(III) to Fe(II) (Fig. S21†).

ROS-generation studies and ferroptosis

The generation of reactive oxygen species (ROS) is a key outcome of the Fenton-type reaction involving iron complexes in the presence of molecular oxygen ($^3\text{O}_2$). These ROS species encompass the superoxide ion (O_2^-), hydrogen peroxide (H_2O_2), and hydroxyl radicals ($^{\bullet}\text{OH}$). Free Fe^{2+} ions serve as generators of ROS, a pivotal factor in the activation of ferroptosis. In the present studies, we utilized the $(\text{Fe}^{\text{III}}\text{T-CATL})^{3-}$ to investigate hydroxyl radical generation, considering the ferroptosis phenomenon following iron(III) leaching *via* the tris catecholate ligand ($\text{H}_6\text{-T-CATL}$), resulting in the formation of an iron(III)-catecholate complex, $(\text{Fe}^{\text{III}}\text{T-CATL})^{3-}$. Hydroxyl radical generation from $(\text{Fe}^{\text{III}}\text{T-CATL})^{3-}$ was probed using a previously established protocol.^{43–45} Initially, benzoic acid, $[\text{Fe}(\text{NO}_3)_3 \cdot 9\text{H}_2\text{O}]$, and $(\text{Fe}^{\text{III}}\text{T-CATL})^{3-}$ were incubated, and UV-visible spectral traces were recorded with increasing concentrations of GSH. The release of Fe^{2+} in the presence of GSH from complex Fe facilitated the formation of $^{\bullet}\text{OH}$ radicals *via* Fenton-like chemistry, reacting with benzoic acid to yield salicylic acid and ultimately forming an iron(III)-salicylate complex (Fig. 4). Several control experiments were conducted in the absence of $(\text{Fe}^{\text{III}}\text{T-CATL})^{3-}$ or GSH confirming that hydroxyl ($^{\bullet}\text{OH}$) radical generation primarily resulted from the reduced- $(\text{Fe}^{\text{II}}\text{T-CATL})^{4-}$ complex. The formation of hydroxyl radicals from the reduced- $(\text{Fe}^{\text{II}}\text{T-CATL})^{4-}$ in the presence of molecular oxygen was further characterized by EPR spectroscopy (Fig. S14†). Hydroxyl radicals were trapped using 5,5-dimethyl-1-pyrrolidine (DMP) to form hydroxylated 5,5-dimethyl-1-pyrrolidine (DMP-OH). The typical EPR spectra of

DMPO-OH species was detected when $(\text{Fe}^{\text{III}}\text{T-CATL})^{3-}$ (50 μM) and GSH (50 μM) were reacted in the presence of 5,5-dimethyl-1-pyrroline N-oxide (DMPO, 0.04 M) in DMF-H₂O (1 : 1, v/v), exhibiting *g*-values of 2.05–2.01.⁴⁶

Glutathione (GSH) depletion assay

To confirm the chemical activation of ferroptosis, we investigated glutathione (GSH) depletion by $^{\bullet}\text{OH}$ radicals, which was identified as a crucial factor in ferroptosis induction. The GSH plays a pivotal role in reducing lipid hydroperoxides to lipid alcohols with the assistance of the GPX4 enzyme.⁴⁷ However, in a ROS-rich environment, GSH is utilized for scavenging ROS, impeding its function in lipid hydroperoxide reduction.⁴⁸ Consequently, the activity of GPX4 is downregulated, leading to increased lipid peroxidation levels and ferroptosis. The ability of the $\text{H}_6\text{-T-CATL}$ in GSH depletion was studied following a previously published protocol by DTNB assay⁴⁹ with a minor modification involving the use of ascorbic acid as a reducing agent to release iron as Fe^{2+} from the $(\text{Fe}^{\text{III}}\text{T-CATL})^{3-}$ (Fig. 5). Focusing on the ferroptosis phenomenon after iron(III) leaching by the tris catecholate ligand ($\text{H}_6\text{-T-CATL}$) to form the iron(III)-catecholate complex, $(\text{Fe}^{\text{III}}\text{T-CATL})^{3-}$, we specifically examined the capacity of $(\text{Fe}^{\text{III}}\text{T-CATL})^{3-}$ to deplete GSH, by employing Ellman's reagent [DTNB = 5,5'-dithiobis-(2-nitrobenzoic acid)]. The reaction between GSH and DTNB results in the formation of an oxidized GS-TNB adduct and a TNB chromophore was characterized by a λ_{max} of 412 nm in the UV-visible spectra. By monitoring the absorbance at 412 nm, indicative of TNB formation, the GSH concentration can be determined. A standard curve was constructed using known GSH concentrations ranging from 0 to 55 μM to determine the overall GSH concentration in unknown analytes. Initially, we incubated 200 μM of ascorbic acid and 55 μM of DTNB in a 5% DMSO-PBS buffer medium (pH = 7.4) to ascertain the

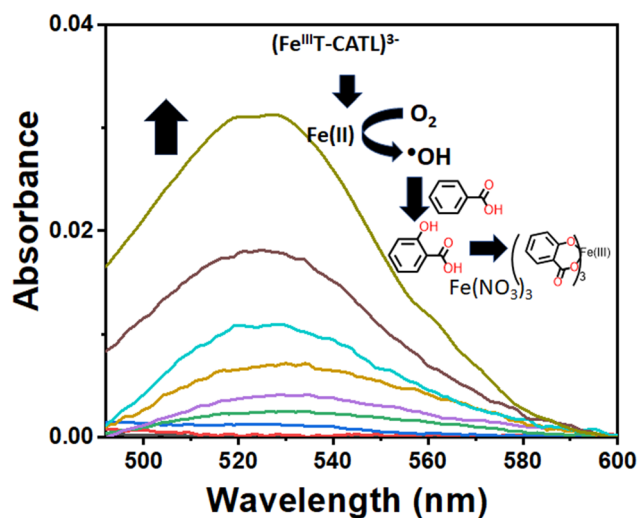


Fig. 4 UV-visible spectroscopic studies for the generation of hydroxyl radical by $(\text{Fe}^{\text{III}}\text{T-CATL})^{3-}$ complex (0.3 mM) in presence of $\text{Fe}(\text{NO}_3)_3 \cdot 9\text{H}_2\text{O}$ (0.2 mM), benzoic acid (0.2 mM), and increasing concentration of GSH (0–10 mM) in 5% DMSO–PBS buffer at pH 7.4 at 298 K. Appearance of typical LMCT band at 520 nm was indicative of the generation of hydroxyl radicals which potentially induced ferroptosis.

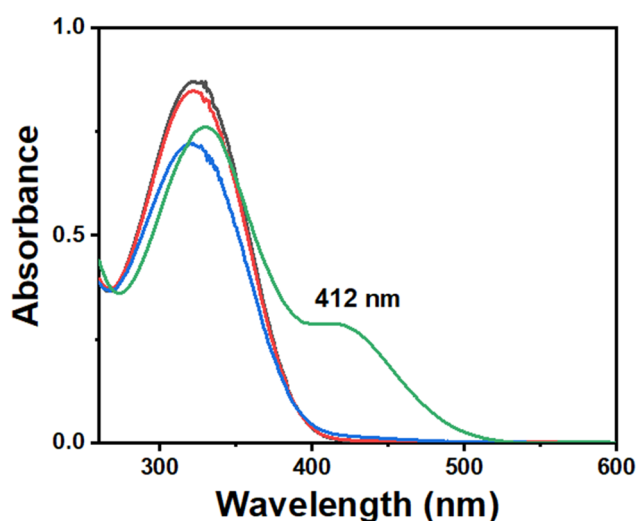


Fig. 5 UV-visible spectral traces of DTNB assay for showing GSH depletion by $(\text{Fe}^{\text{III}}\text{T-CATL})^{3-}$ complex (0.1 mM) in 5% DMSO–PBS buffer medium at pH 7.4 and room temperature.

reduction of DTNB by ascorbic acid. Subsequently, 100 μM of $(\text{Fe}^{\text{III}}\text{T-CATL})^{3-}$ was added, followed by 50 μM of GSH. The UV-visible spectra were recorded every 10 minutes of incubation. The concentration of GSH in each sample was determined based on absorbance values measured at 412 nm using the standard curve. The extent of GSH depletion was calculated by subtracting the corresponding GSH concentration from the initial 50 μM concentration in the sample. The observed depletion of 31 μM GSH was due to the generation of hydroxyl radicals by Fe^{2+} in the presence of molecular oxygen underscoring the potential role of $(\text{Fe}^{\text{III}}\text{T-CATL})^{3-}$ in inducing ferroptosis.

BSA binding studies

Typically constituting approximately 60% of blood plasma proteins, serum albumin plays pivotal roles in maintaining blood pH and facilitating the transport of various ligands, molecules, and drugs throughout the bloodstream. In this investigation, we conducted a fluorometric assay to explore the potential interaction between the tris-catecholate ligand (T-CATL) and bovine serum albumin (BSA), serving as a model for human serum albumin (HSA) (Fig. S12[†]). BSA exhibits strong fluorescence owing to luminescent amino acid residues—tryptophan (Trp), tyrosine (Tyr), and phenylalanine (Phe). The fluorescence emission of BSA, excited at 280 nm, was observed at approximately 339 nm.^{50,51} Throughout the experiment, $\text{H}_6\text{-T-CATL}$ (0.001 M, stock) was incrementally added to a BSA solution with a concentration of 3.0×10^{-5} M. The findings revealed that the emission of BSA at 339 nm was quenched upon binding with $\text{H}_6\text{-T-CATL}$, leading to a slight blue shift of $\Delta\lambda = 3\text{--}7$ nm. The binding constant derived from Stern–Volmer and Scatchard plots was determined to be $3.98 \times 10^4 \text{ mol}^{-1}$, with a calculated Gibbs free energy of $-6.27 \text{ kcal mol}^{-1}$ (Fig. S12[†]). These results suggest a robust interaction between $\text{H}_6\text{-T-CATL}$ and serum albumin protein, indicating favourable conditions for enhanced transport of ligand ($\text{H}_6\text{-T-CATL}$) in the bloodstream.

Cell viability, apoptosis, and DNA damage responses

$\text{H}_6\text{-T-CATL}$ exhibited cytotoxicity against A549 lung cancer cells with an IC_{50} of 14.19 μM while in MDA-MB-231 breast cancer cells the IC_{50} was 20.23 μM (Table S1[†]). This difference in cytotoxicity between the two cancer cell lines may be attributed to the relatively higher concentration of glutathione in A549 cells, which is believed to trigger ferroptosis in cancer cells. Furthermore, the cytotoxicity of $\text{H}_6\text{-T-CATL}$ in normal cells like HEK293 (kidney cells) and AC16 (human heart cells) yielded an IC_{50} value of greater than 80 μM respectively, indicating a significantly lower level of toxicity compared to the cancer cell lines (Fig. 6).⁵² This difference in level of cytotoxicity could be due to the reduced uptake of $\text{H}_6\text{-T-CATL}$ in normal cells, highlighting the selective toxicity of $\text{H}_6\text{-T-CATL}$ towards cancer cells. Our findings further revealed that after treatment with ligand ($\text{H}_6\text{-T-CATL}$), cell viability was 51.26% in live cells, 40.78% in early apoptotic cells, 7.94% in late apoptotic cells, and 0.02% in necrotic cells (Fig. 6) indicating the involvement

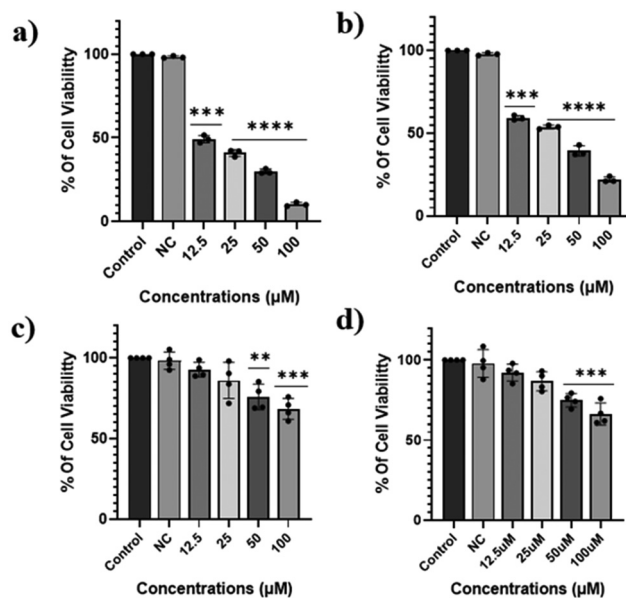


Fig. 6 (a) Cell viability (MTT assay) plots showing the cytotoxicities of the ligand (T-CATL) in the (a) A549, (b) MDA-MB-231, (c) HEK293, and (d) AC16 cell lines. All data are presented as means \pm S.E. of multiple experiments ($n = 4$, ns indicates nonsignificant and $*p < 0.05$, $**p < 0.01$, $***p < 0.001$, $****p < 0.0001$ compared to the control group). NC was used as a negative control [cell treated with DMSO–PBS].

of apoptotic signaling in the $\text{H}_6\text{-T-CATL}$ -induced cellular phenotype (Fig. 7).⁵³

The involvement of oxidative processes was also confirmed as evidenced by the generation of ROS and subsequent cellular signaling. The cells with $\text{H}_6\text{-T-CATL}$ treatment undergo activation of DNA damage signaling response, initiated by phosphorylation of histone H2AX (γH2AX) at the site of the double-stranded break and leads to recruitment of ATM (ataxia-telangiectasia mutated kinase). This signaling promotes cell death *via* up-regulation of various apoptotic marker proteins such as Bax (Bcl-2-associated protein x), p53, PUMA (p53 upregulated modulator of apoptosis) together with downregulation of anti-apoptotic proteins Bcl2 (B-cell leukemia/lymphoma 2 protein) (Fig. S22[†]).⁵⁴

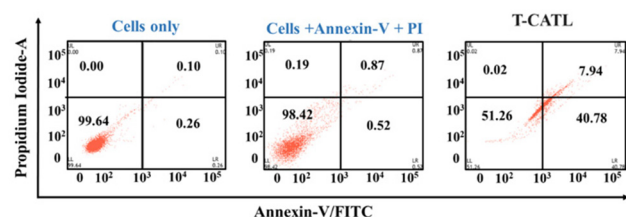


Fig. 7 Annexin-V FITC/PI assay in A549 cells was cultured with ligand ($\text{H}_6\text{-T-CATL}$) at a concentration of 37 μM for 4 hours. Appropriate controls with cells alone and cells treated with only annexin and PI. The respective quadrants represent the percentage (%) of the cell population (lower left: live; lower right: early apoptotic; upper right: late apoptotic; and upper left: dead cells).

The tumor suppressor protein, p53 directly interacts with pro-apoptotic protein Bax or PUMA which in turn counterbalances the anti-apoptotic protein Bcl2. The proportion of Bax to Bcl2 regulated the mitochondrial permeability transition pore that leads to mitochondrial dysfunction *via* decreasing mitochondrial membrane potential (MMP, $\Delta\tilde{N}_{\pm m}$). This mechanism eventually causes cell death including ferroptosis by releasing ROS. Indeed, we observed that the introduction of compound ligands to cancer cells significantly increased intracellular ROS, and reduced MMP simultaneously with increased immunoreactivity for markers of ferroptosis like malondialdehyde (MDA) and 4-hydroxynonenal (4HNE) (Fig. S23†).⁵² MDA & 4HNE also play a vital role in the suppression of anti-apoptotic protein Bcl2 and promote a feed-forward loop towards promoting ferroptosis in the cellular system. Altogether, our data suggest that H₆-T-CATL significantly initiates ferroptosis-mediated signaling events in cancer cells that induce DNA damage responses.

Experimental

Materials and methods

[Fe(NO₃)₃·9H₂O], FeCTPTP·4H₂O, 1*H*-pyrrole, 4-methyl benzaldehyde, propionic acid, triethylamine, trifluoroacetic acid (TFA), L-Dopa, EDC·HCl, HOBT, di-*tert*-butyl dicarbonate, MTT, BSA, 1,10-phenanthroline, sodium hydroxide, and sodium chloride were procured from Sigma-Aldrich (USA). Dopamine·HCl, L-ascorbic acid, glutathione reduced (GSH), and DTNB were obtained from SRL Chemical Company (India). Other chemicals and solvents were sourced from TCI Chemicals, Alfa-Aesar, HI-MEDIA, and Finnar Chemicals and were utilized without further purification.

UV-visible spectra of the compounds and UV-visible spectroscopic experiments were conducted using a PerkinElmer UV-visible spectrophotometer. The IR spectra were recorded using a PerkinElmer UATR Two FT-IR spectrophotometer. Cyclic voltammetry studies were performed using Metrohm Autolab Potentiostat. Absorbance measurements during the MTT experiment were taken using a Molecular Devices Versa Max adjustable microplate reader. The IUPAC designation and creation of compound structures were carried out using Chem Draw Professional 15. The DCFDA and annexin-V/PI assays were analyzed utilizing fluorescence-activated cell sorting (FACS) analysis using the BD FACS-Verse Flow Cytometer.

Synthesis

The *meso*-substituted porphyrin ligand, 5,10,15,20-tetra-*p*-tolylporphyrin (TPTP), was synthesized following established protocols outlined in prior literature and subsequently characterized using UV-visible and IR, spectroscopy (Fig. S3 and S4†).³⁵

Synthesis of tris catechololate ligand (H₆-T-CATL).^{33,34} The previously published synthesis protocol was employed to synthesize the tris catechololate ligand, designated as H₆-T-CATL, which is chemically identified as 2-amino-*N*-(1-((3,4-dihydroxyphenethyl)amino)-3-(3,4-dihydroxyphenyl)-1-oxopropan-2-yl)-3-

(3,4-dihydroxyphenyl)propenamide. The synthesis procedure involved several steps. Initially, the amine group in L-Dopa was protected using di-*tert*-butyl dicarbonate (BoC). Subsequently, a coupling reaction was performed between the -COOH group of Boc-NH₂-protected L-Dopa and the NH₂ group of dopamine in the presence of 1-ethyl-3-(3-dimethyl aminopropyl)carbodiimide (EDC), hydroxybenzotriazole (HOBT), and triethylamine. The resulting product was then purified using silica gel chromatography. The Boc-protected NH₂ group in this product was deprotected using a mixture of trifluoroacetic acid (TFA) and methylene chloride. Following deprotection, the free NH₂ group of the coupled product underwent another coupling reaction with the -COOH group of Boc-NH₂-protected L-Dopa under similar conditions. The resulting product was again purified by silica gel chromatography. The final product, H₆-T-CATL, was obtained as a brown viscous oily liquid with a yield of 20%. Its FT-IR spectra in the solid phase showed characteristic peaks at ν (cm⁻¹) 3321, 3495, and 1650, corresponding to O-H stretching, N-H stretching, and C=O stretching, respectively. Q-TOF ESI mass analysis in MeOH revealed a peak at *m/z* 512.2061, corresponding to [M + H]⁺ (Fig. S1 and S2†).

Synthesis of Fe-TPP-CTPTP.³⁶ The preparation of the complex (Fe-TPP-Cl) was conducted following a previously established protocol. Initially, a solution of TPTP in DMF was added to a round-bottom flask containing a solution of [FeCTPTP·4H₂O] in DMF under a nitrogen atmosphere with continuous stirring for 15 minutes. The resulting mixture was then subjected to reflux at 170 °C for 6 hours, followed by gradual cooling to room temperature. Subsequently, the dark brown solution obtained was poured into water, leading to the formation of a precipitate, which was collected *via* vacuum filtration. The precipitate was dissolved in dichloromethane (DCM) and transferred to a round-bottom flask, to which a 20 mL solution of 1 M HCl was added. The mixture was vigorously stirred for 14 hours at room temperature. Afterward, the contents of the flask were transferred to a separatory funnel, and the organic phase was washed thrice with water. The organic phase was dehydrated using Na₂SO₄, filtered through a glass frit, and the solvent was evaporated using a rotary evaporator. The crude material obtained was subjected to silica gel column chromatography purification using a mixture of CH₂CTPTP and 1% acetone. The solvent was evaporated under reduced pressure, yielding a dark purple solid.

The complex Fe-TPP-Cl was obtained with a yield of 60%. Its color was dark purple, and its absorption maxima ([λ_{\max} , nm]) were observed at 380 nm, 425 nm, and 511 nm. Q-TOF ESI mass analysis in DMF revealed a peak at *m/z* 760.1937, corresponding to [M + H]⁺ (Fig. S5 and S6†).

Synthesis of Fe. The synthesis of the iron(III)-catechololate complex (Fe) was initiated by adding 6 equivalents (30 μ L) of triethylamine to a 20 mL beaker containing a methanolic solution of ligand (H₆-T-CATL). This solution was then slowly added to a 100 mL round-bottom flask (RB) containing a methanolic solution of [Fe(NO₃)₃·9H₂O] under an inert atmosphere of nitrogen (N₂) with continuous stirring. A notable

color change to dark purple and precipitation occurred upon the dropwise addition of diethyl ether in ice-cooled conditions, leading to the formation of the complex with a yield of 30%. The resulting complex **Fe** exhibited a dark purple color, with UV-visible spectra obtained in 5% DMSO–PBS buffer revealing absorption maxima (λ_{max} , nm) at 330 nm and 570 nm. The solid-phase FT-IR spectra displayed characteristic peaks at ν (cm^{-1}) 3047 (O–H stretching), 3347 (N–H stretching), and 1647 (C=O stretching). Q-TOF ESI mass analysis in MeOH revealed a peak at m/z 187.01245 (Fig. S7–S9†).

Conclusions

The use of the siderophore mimic tris catecholate ligand (**H₆-T-CATL**) to induce ferroptosis is a pioneering anticancer strategy. Our study introduced a novel approach to trigger ferroptosis by extracting iron from Fe-TPP-Cl, mimicking cytochrome, with **H₆-T-CATL**. Experimental evidence demonstrated iron release in the presence of glutathione (GSH) and elucidated pathways involved in ferroptosis induction, including hydroxyl radical generation and GSH depletion. *In vitro* MTT assays on A549 and MDA-MB-231 cancer cell lines showed promising IC₅₀ values towards cell killing. Additionally, ROS generation particularly hydroxyl radicals by ligand (**H₆-T-CATL**) activated the mitochondrial-dependent DNA damage signaling processes and elevated the levels of different protein expressions that promote ferroptosis. Further, **H₆-T-CATL** promoted a significant apoptotic cell death-inducing feed-forward loop that generates more ROS and propagates DNA damage-induced signaling. In summary, our study unveils a groundbreaking anticancer pathway integrating chelation therapy with ferroptosis induction coupled to oxidative stress-dependent cellular phenotype. Strategic iron manipulation and ROS modulation with **H₆-T-CATL** offer promising prospects for effective anticancer treatments, emphasizing ferroptosis as a targeted cell eradication mechanism.

Author contributions

Abhishek Panwar: execution of the project, synthesis, and characterization, photophysical studies, writing – original draft, Biswanath Maity: *in vitro* assays and protein assays, Dulal Musib: *in vitro* assays, Anushree Lye: *in vitro* assays, Aarti Upadhyay: *in vitro* assays; Karan: ferroptosis chemical studies, Bebika: binding constant studies, Maynak Pal: data collection and experimental studies, Mithun Roy: conceptualization, fund accumulation, supervision of the work, writing – original draft and editing.

Data availability

The data supporting this article have been included as part of the ESI.†

Conflicts of interest

There are no conflicts to declare.

Acknowledgements

MR thanks the Board of Research in Nuclear Sciences (BRNS), Mumbai (37(2)/14/18/2017-BRNS), Indian Council of Medical Research (ICMR) (R.11.13/42/2021-GIA/HR, ICMR), SERB (CRG/2021/004337) for financial support. BM also acknowledges SERB for the financial support (CRG/2022/003455). The authors thank NIT Manipur and CBMR Lucknow for the infrastructural support. They also sincerely thank Prof. Akhil R. Chakravarty, IISc Bangalore for helping part in the cell culture experiments and Punjab University for the characterizations.

Notes and references

- 1 S. V. Torti and F. M. Torti, *Nat. Rev. Cancer*, 2013, **13**, 342–355.
- 2 S. Liu, X. Cao, D. Wang and H. Zhu, *Arch. Biochem. Biophys.*, 2022, **723**, 109199.
- 3 T. Basak and R. K. Kanwar, *Cancer Med.*, 2022, **11**, 3837–3853.
- 4 A. Fonseca-Nunes, P. Jakszyn and A. Agudo, *Cancer Epidemiol., Biomarkers Prev.*, 2014, **23**, 12–31.
- 5 S. V. Torti and F. M. Torti, *Mol. Aspects Med.*, 2020, **75**, 100860.
- 6 D. H. Manz, N. L. Blanchette, B. T. Paul, F. M. Torti and S. V. Torti, *Ann. N. Y. Acad. Sci.*, 2016, **1368**, 149–161.
- 7 F. Ding, L. Zhang, H. Chen, H. Song, S. Chen and H. Xiao, *Nanoscale Horiz.*, 2020, **5**, 999–1015.
- 8 M. El Hout, L. Dos Santos, A. Hamaï and M. Mehrpour, *Semin. Cancer Biol.*, 2018, **53**, 125–138.
- 9 L. Zhou, B. Zhao, L. Zhang, S. Wang, D. Dong, H. Lv and P. Shang, *Int. J. Mol. Sci.*, 2018, **19**, 1545.
- 10 M. Prutki, M. Poljak-Blazi, M. Jakopovic, D. Tomas, I. Stipancic and N. Zarkovic, *Cancer Lett.*, 2006, **238**, 188–196.
- 11 J. Buss, F. Torti and S. Torti, *Curr. Med. Chem.*, 2003, **10**, 1021–1034.
- 12 M. Whitnall, J. Howard, P. Ponka and D. R. Richardson, *Proc. Natl. Acad. Sci. U. S. A.*, 2006, **103**, 14901–14906.
- 13 A. Khan, P. Singh and A. Srivastava, *Microbiol. Res.*, 2018, **212–213**, 103–111.
- 14 R. C. Hider and X. Kong, *Nat. Prod. Rep.*, 2010, **27**, 637.
- 15 C. Kurth, H. Kage and M. Nett, *Org. Biomol. Chem.*, 2016, **14**, 8212–8227.
- 16 A. Steinbrueck, A. C. Sedgwick, H.-H. Han, M. Y. Zhao, S. Sen, D.-Y. Huang, Y. Zang, J. Li, X.-P. He and J. L. Sessler, *Chem. Commun.*, 2021, **57**, 5678–5681.
- 17 G. J. Kontoghiorghes and C. N. Kontoghiorghes, *Drug Des., Dev. Ther.*, 2016, 465.

- 18 M. R. Bedford, S. J. Ford, R. D. Horniblow, T. H. Iqbal and C. Tselepis, *J. Clin. Pharmacol.*, 2013, **53**, 885–891.
- 19 G. Jones, S. K. Goswami, H. Kang, H. S. Choi and J. Kim, *Nanomedicine*, 2020, **15**, 1341–1356.
- 20 Y. Chen, X. Guo, Y. Zeng, X. Mo, S. Hong, H. He, J. Li, S. Fatima and Q. Liu, *Sci. Rep.*, 2023, **13**, 1–14.
- 21 D. Tang, X. Chen, R. Kang and G. Kroemer, *Cell Res.*, 2020, **31**, 107–125.
- 22 J. Li, F. Cao, H. Yin, Z. Huang, Z. Lin, N. Mao, B. Sun and G. Wang, *Cell Death Dis.*, 2020, **11**, 1–13.
- 23 L. Wang, X. Chen and C. Yan, *Genes Dis.*, 2022, **9**, 334–346.
- 24 Y. Ming, M. Huang, Y. Huang, D. Liu, M. Sun, B. Jia and J. Du, *Mater. Chem. Front.*, 2024, **8**, 1685–1702.
- 25 M. Antoszczak, S. Müller, T. Cañeque, L. Colombeau, N. Dusetti, P. Santofimia-Castaño, C. Gaillet, A. Puisieux, J. L. Iovanna and R. Rodriguez, *J. Am. Chem. Soc.*, 2022, **144**, 11536–11545.
- 26 H. Yu, J. Yan, Z. Li, L. Yang, F. Ju and Y. Sun, *Nanoscale Adv.*, 2023, **5**, 1271–1290.
- 27 D. Xiang, L. Zhou, R. Yang, F. Yuan, Y. Xu, Y. Yang, Y. Qiao and X. Li, *Int. J. Nanomed.*, 2024, **19**, 2091–2112.
- 28 C. Liang, X. Zhang, M. Yang and X. Dong, *Adv. Mater.*, 2019, **31**, 1–25.
- 29 A. Ghoochani, E.-C. Hsu, M. Aslan, M. A. Rice, H. M. Nguyen, J. D. Brooks, E. Corey, R. Paulmurugan and T. Stoyanova, *Cancer Res.*, 2021, **81**, 1583–1594.
- 30 Q. Nie, Y. Hu, X. Yu, X. Li and X. Fang, *Cancer Cell Int.*, 2022, **22**, 1–19.
- 31 Y. Zou and S. L. Schreiber, *Cell Chem. Biol.*, 2020, **27**, 463–471.
- 32 J. Liu, R. Kang and D. Tang, *Trends Cancer*, 2024, **10**, 417–429.
- 33 T. Gillich, E. M. Benetti, E. Rakhmatullina, R. Konradi, W. Li, A. Zhang, A. D. Schlüter and M. Textor, *J. Am. Chem. Soc.*, 2011, **133**, 10940–10950.
- 34 R. Larsson, N. Blanco, M. Johansson and O. Sterner, *Tetrahedron Lett.*, 2012, **53**, 4966–4970.
- 35 R. Soury, M. Chaabene, M. Jabli and Y. Rousselin, *J. Solid State Chem.*, 2021, **295**, 121920.
- 36 Z.-C. Sun, Y.-B. She, Y. Zhou, X.-F. Song and K. Li, *molecules*, 2011, **16**, 2960–2970.
- 37 D. Roy, A. Chakraborty and R. Ghosh, *RSC Adv.*, 2017, **7**, 40563–40570.
- 38 Z. Hou, T. D. P. Stack, C. J. Sunderland and K. N. Raymond, *Inorg. Chim. Acta*, 1997, **263**, 341–355.
- 39 Y. Zhao, X. Cai, Y. Zhang, C. Chen, J. Wang and R. Pei, *Nanoscale*, 2019, **11**, 12250–12258.
- 40 J. Oh, D. Kang, S. Hong, S. H. Kim, J.-H. Choi and J. Seo, *Dalton Trans.*, 2021, **50**, 3459–3463.
- 41 E. Agustina, J. Goak, S. Lee, Y. Seo, J. Park and N. Lee, *ChemistryOpen*, 2015, **4**, 613–619.
- 42 L. G. Bachas, L. Cullen, R. S. Hutchins and D. L. Scott, *J. Chem. Soc., Dalton Trans.*, 1997, 1571–1578.
- 43 P. Kord Forooshani, R. Pinnaratip, E. Polega, A. G. Tyo, E. Pearson, B. Liu, T.-O. Folayan, L. Pan, R. M. Rajachar, C. L. Heldt and B. P. Lee, *Chem. Mater.*, 2020, **32**, 8182–8194.
- 44 X. Sui, J. Wang, Z. Zhao, B. Liu, M. Liu, M. Liu, C. Shi, X. Feng, Y. Fu, D. Shi, S. Li, Q. Qi, M. Xian and G. Zhao, *Commun. Biol.*, 2024, **7**, 199, DOI: [10.1038/s42003-024-05903-5](https://doi.org/10.1038/s42003-024-05903-5).
- 45 S. Gazi and R. Ananthkrishnan, Semi-Quantitative Determination of Hydroxyl Radicals by Benzoic Acid Hydroxylation: An Analytical Methodology for Photo-Fenton Systems, *Curr. Anal. Chem.*, 2012, **8**, 143.
- 46 M. Pal, A. Upadhyay, N. Masarkar, A. Bera, S. Mukherjee and M. Roy, *Dalton Trans.*, 2024, **53**, 2108–2119.
- 47 R. L. Bertrand, *Med. Hypotheses*, 2017, **101**, 69–74.
- 48 B. Niu, K. Liao, Y. Zhou, T. Wen, G. Quan, X. Pan and C. Wu, *Biomaterials*, 2021, **277**, 121110.
- 49 R. Bhowmik, A. Upadhyay, M. Pal, A. Bera and M. Roy, *New J. Chem.*, 2024, **48**, 5465–5474.
- 50 T. Topalá, A. Bodoki, L. Oprean and R. Oprean, *Med. Pharm. Rep.*, 2014, **87**, 215–219.
- 51 V. D. Suryawanshi, L. S. Walekar, A. H. Gore, P. V. Anbhule and G. B. Kolekar, *J. Pharm. Anal.*, 2016, **6**, 56–63.
- 52 S. Sivagnanam, K. Das, M. Basak, T. Mahata, A. Stewart, B. Maity and P. Das, Self-assembled dipeptide based fluorescent nanoparticles as a platform for developing cellular imaging probes and targeted drug delivery chaperones, *Nanoscale Adv.*, 2022, **4**, 1694–1706.
- 53 D. Musib, M. Pal, M. K. Roy and M. Raza, Photo-physical, theoretical and photo-cytotoxic evaluation of a new class of lanthanide(III)-curcumin/diketone complexes for PDT application, *Dalton Trans.*, 2020, **49**, 10786–10798.
- 54 M. Basak, K. Das, T. Mahata, A. S. Sengar, S. K. Verma, S. Biswas, K. Bhadra, A. Stewart and B. Maity, RGS7-ATF3-Tip60 Complex Promotes Hepatic Steatosis and Fibrosis by Directly Inducing TNF α , *Antioxid. Redox Signaling*, 2023, **38**, 137–159.